

**Pre-impact mutual orbit of the DART target
binary asteroid (65803) Didymos derived from
observations of mutual events in 2003–2021**

2 Abstract

3 We modeled photometric observations of mutual events (eclipses and occultations)
4 between the components of the binary near-Earth asteroid (65803) Didymos, the
5 target of the Double Asteroid Redirection Test (DART) space mission, that were
6 taken from 2003 to 2021 (Pravec et al. 2022, submitted). We derived parameters
7 of the modified Keplerian mutual orbit (allowing for a quadratic drift in the mean
8 anomaly, which is presumably caused by **an interplay between the BYORP
9 effect and mutual tides, or by differential Yarkovsky force**) of the secondary,
10 called Dimorphos, around the Didymos primary and estimated its diameter. The
11 J2000 ecliptic longitude and latitude of the orbital pole are $320.6^\circ \pm 13.7^\circ$ and
12 $-78.6^\circ \pm 1.8^\circ$, respectively, and the orbital period is 11.921624 ± 0.000018 h at
13 epoch JD 2455873.0 (asterocentric UTC; all quoted uncertainties correspond to
14 3σ , **except the density estimate below**). We obtained the quadratic drift of
15 the mean anomaly of 0.15 ± 0.14 deg/yr². The orbital eccentricity is ≤ 0.03 . We
16 determined the ecliptic longitude and latitude of the radius vector of Dimorphos
17 with respect to Didymos at the nominal time of the DART impact to Dimorphos (JD
18 2459849.46875 geocentric UTC) to be $222.8^\circ \pm 7.0^\circ$ and $-1.6^\circ \pm 4.2^\circ$, respectively.
19 **We also estimated the bulk density of the system to be 2.44 ± 0.30 g cm⁻³**
20 **(1 σ uncertainty).**

21 *Key words:* Asteroids, satellites; Photometry; DART space mission; Hera space
22 mission

24 The near-Earth asteroid (65803) Didymos, originally designated 1996 GT, was dis-
25 covered by the *Spacewatch* asteroid survey from Kitt Peak Observatory in Arizona
26 on 1996 April 11. Its binary nature was revealed by Pravec et al. (2003). Pravec et
27 al. (2006) and Scheirich and Pravec (2009) analyzed and modeled photometric data
28 obtained during its close approach to Earth in 2003. They reported initial estimates
29 of the binary system properties, including parameters of the mutual orbit of the two
30 components. The system was also observed using radar from Arecibo and Goldstone
31 in 2003. The radar observations were published and modeled together with the pho-
32 tometric data by Naidu et al. (2020) who obtained a shape model of the primary
33 and determined or constrained several parameters of the binary asteroid system.

34 Didymos is classified as an S-type asteroid (Cheng et al., 2018) based on vis-IR
35 spectra obtained by de León et al. (2010), also confirmed by Dunn et al. (2013).

36 The secondary of the Didymos binary system, recently named Dimorphos, has been
37 selected as a target of the Double Asteroid Redirection Test (DART). It is NASA’s
38 first planetary defense test mission, **with the goal of demonstrating the kinetic**
39 **impactor mitigation technique on an asteroid.** It was launched in November
40 2021, and it will **arrive at** the Didymos system on the **September 26, 2022** at
41 23:15 UTC and impact into Dimorphos. The main benefit of **targeting** a binary
42 asteroid system **on a** kinetic impactor mission is that it allows **the main result**
43 **of the test – the change in the mutual orbital period –** to be measured
44 from Earth via photometric observations, assuming that the binary system exhibits
45 mutual events seen from Earth (**Cheng et al., 2015**). Rivkin et al. (2021) discuss
46 the factors that led to the recognition that Didymos was the best candidate for
47 a kinetic impactor test, and its selection as the DART **target. The Didymos**
48 **system will be investigated by ESA’s Hera mission from the beginning**
49 **of 2027 for about half a year, which** will provide a thorough description of the
50 post-impact state of the binary system (Michel et al., 2022).

51 An important part of the preparation of the DART mission has been an observa-
52 tional effort to precisely determine the orbit of the secondary around the primary.
53 For that, Pravec et al. (2022) obtained photometric observations of **the** Didymos
54 system taken with several large- or medium-sized groundbased telescopes from 2015
55 to 2021. In this paper, we present results from mutual orbit modeling using the com-
56 plete photometry data for mutual events in the Didymos system from 2003 to 2021.
57 An independent derivation of the mutual orbit based on an analysis of mutual event
58 timings has been made by Naidu et al. (**2022**).

59 2 Mutual orbit model of Didymos system

60 2.1 Observational data

61 The data used in our analysis, obtained during five apparitions of Didymos from
62 2003 to 2021, were published in Pravec et al. (2006, 2022). We briefly summarize
63 them in Table 1. Each row in the table represents one apparition, identified with the
64 mid-UTC date of its first and last observing **sessions (runs)** rounded to the nearest
65 tenth of a day in the first column. Subsequent columns give the number of observing
66 runs (labeled as *No. of nights*, but we note that they were taken using several
67 telescopes and so more than one run was sometimes taken on a single night) in the
68 given apparition and a reference to where more information on the observations is
69 available.

70 The data were analysed using the standard technique described in Pravec et al.
71 (2006, 2022). **Briefly, by fitting a two-period Fourier series to data points
72 taken outside mutual (occultation or eclipse) events, the rotational lightcurves
73 of the primary and the secondary, which are additive in flux units, are
74 separated. Subtracting the rotational lightcurve of the primary from the
75 data, a long-period (orbital) lightcurve component containing the mutual
76 events and the secondary rotation lightcurve is obtained, which is then
77 used for subsequent numerical modeling.** We refer the reader to Pravec et al.
78 (2022) for details of the lightcurve decomposition method.

Table 1

Photometric observations of the Didymos system

Time span	No. of nights	Reference
2003-11-20.9 to 2003-12-20.3	17	P06
2015-04-13.3 to 2015-04-14.4	2	P22
2017-02-23.3 to 2017-05-04.3	13	P22
2019-01-31.4 to 2019-03-11.1	5	P22
2020-12-12.6 to 2021-03-06.3	15	P22

References: P06 (Pravec et al., 2006), P22 (Pravec et al., 2022)

79 2.2 Numerical model

80 We constructed the model of the Didymos system using the technique of Scheirich
81 and Pravec (2009) which was further developed by Scheirich et al. (2015, 2021). In
82 the following, we outline the basic points of the method, but we refer the reader to
83 the 2009, 2015, and 2021 papers for details of the technique.

84 The binary asteroid components were represented with spheres or oblate (for the
85 primary) and prolate (for the secondary) ellipsoids (the ellipsoidal shapes were used
86 to check the sensitivity of the solution to the shapes of the components, see below),

87 orbiting each other on a circular orbit. We choose the circular orbit for simplicity,
 88 as the upper limit on the eccentricity is low (see below). The motion was assumed
 89 to be Keplerian, but we allowed for a quadratic drift in the mean anomaly. The spin
 90 axis of the primary was assumed to be normal to the mutual orbital plane of the
 91 components (i.e., we assumed zero inclination of the mutual orbit. **See Appendix**
 92 **A for an assessment of this assumption.**). When the secondary was modeled as
 93 the prolate spheroid, its long axis was kept aligned with the centers of the two bodies
 94 (i.e., in synchronous rotation with zero libration). The shapes were approximated
 95 with 1016 and 252 triangular facets for the primary and the secondary, respectively.
 96 The components were assumed to have the same albedo **and to be exempt from**
 97 **albedo features (see Kaasalainen and Torppa, 2001, for discussion on why**
 98 **albedo features can be neglected).** The brightness of the system as seen by the
 99 observer was computed as a sum of contributions from all visible facets using a
 100 ray-tracing code that checks which facets are occulted by or are in shadow from the
 101 other body. A combination of Lommel-Seeliger and Lambert scattering laws was
 102 used (see, e.g., Kaasalainen et al., 2002).

103 The quadratic drift in the mean anomaly, ΔM_d , was fitted as an independent pa-
 104 rameter. It is the coefficient in the second term of the expansion of the time-variable
 105 mean anomaly:

$$106 \quad M(t) = M(t_0) + n(t - t_0) + \Delta M_d(t - t_0)^2, \quad (1)$$

107 where

$$108 \quad \Delta M_d = \frac{1}{2} \dot{n}, \quad (2)$$

109 where n is the mean motion, t is the time, and t_0 is the epoch. ΔM_d was stepped
 110 from -10 to $+10$ deg/yr² with a step of 0.01 deg/yr², and all other parameters were
 111 fitted at each step.

112 Since the $3\text{-}\sigma$ upper limit on the eccentricity of the mutual orbit is 0.03 only
 113 (Scheirich and Pravec, 2009), we set the eccentricity equal to zero for simplicity
 114 and efficiency. This assumption had a negligible effect on the accuracy of other de-
 115 rived parameters of the models. Scheirich and Pravec (2009) estimated the upper
 116 limit on the eccentricity using the data from the 2003 apparition. We checked that
 117 their upper limit is consistent with the data taken in 2015 to 2021, but those later
 118 data do not possess the characteristics necessary to use them for constraining the
 119 eccentricity more. Those characteristics include sufficient quality, time coverage, and
 120 depths of the mutual events. Thus, the constraint on the eccentricity by Scheirich
 121 and Pravec (2009) still applies.

122 Except for the data quality, constraining the eccentricity is also **limited by pres-**
 123 **ence of systematic modeling errors for the timings** of mutual events. **The**
 124 **model systematics are** caused by the simplification of the shape of the primary
 125 (see below and Fig. 9), **which can be up to 5 minutes for the Didymos sys-**
 126 **tem. Generally, mutual events between bodies on an eccentric orbit occur**
 127 **at times that are offset from the times of events for a circular orbit.** For

128 eccentricity of 0.03, these offsets are **between 0 and 5 minutes** (corresponding
 129 **to between 0 and 2.5°** in the mean anomaly of the secondary) for **near-central**
 130 **events** occurring close to the primary’s equator and **between 0 and 8 minutes**
 131 **(between 0 and 5° in mean anomaly)** for **non-central** events occurring close to
 132 the primary’s pole. The magnitude of **the systematic modeling errors** is compa-
 133 rable to the magnitude of **event time offsets caused by non-zero eccentricity,**
 134 **so they can be confused. To reduce the effect of the systematic modeling**
 135 **errors on eccentricity estimation, either a high number of mutual events**
 136 **would have to be observed so that we get a set of event timings taken**
 137 **at many different primary rotational phases that would average out the**
 138 **shape modeling errors, or use a detailed shape model for the primary**
 139 **(which may be constructed from resolved images that will be taken by**
 140 **DART).**

141 Across all observations, we found a unique solution for the system parameters, see
 142 Table 2. We describe and discuss these parameters in Section 3.

143 We estimated uncertainties of the fitted parameters using two techniques. The un-
 144 certainties of the relative semimajor axis and the orbital pole (these parameters are
 145 strongly determined by the shapes of the mutual events) were estimated using the
 146 procedure described in Scheirich and Pravec (2009). The uncertainties of the rest of
 147 the parameters, which are determined primarily by the timings of the events, were
 148 estimated using the method described in Scheirich et al. (2021), which we outline
 149 below.

150 The residuals of the model fitted to the observational data do not obey the Gaus-
 151 sian statistics because of systematic errors resulting from model simplifications. In
 152 particular, the residuals of nearby measurements appear correlated. To eliminate
 153 the effect we adopted the following strategy based on the χ^2 test.

154 We choose a correlation time d and for each data point (i) we calculated how many
 155 other data points, K_i , are within $\pm d/2$ from the given point. We then applied a
 156 weight of $1/K_i$ to the given data point in the χ^2 sum. We also calculated an effective
 157 number of data points as $N_{\text{eff}} = \sum_{i=1}^N 1/K_i$, where N is the total number of data
 158 points. For normalized χ^2 we then have $\chi^2 = 1/(N_{\text{eff}} - M) \sum_{i=1}^N (O - C)_i^2 / (\sigma_i^2 K_i)$,
 159 where M is the number of fitted parameters of the model and σ_i is a standard
 160 deviation of the i th point. As the residuals are predominated by model rather than
 161 observational uncertainties, we assign each data point the same standard deviation
 162 $\sigma_i = \sigma$, where σ is the RMS residual (root mean square of observed magnitudes,
 163 O , minus the values calculated from the model, C) of the best fit solution. **An**
 164 **illustration of the weights $1/K_i$ determination is shown in Fig. 1. In Fig. 2,**
 165 **the distribution of residuals with and without the weights applied is**
 166 **shown for comparison.**

167 The procedure described above is equivalent to reducing the number of data points
 168 to one in each time interval with the length d (i.e., to reducing the total number
 169 of points to N_{eff}) and assigning $(O - C)^2$ of this point to be a mean of $(O_i - C_i)^2$
 170 of all the points within the interval. However, our approach has the advantage that
 171 it does not depend on a particular realization of dividing the observing time span

172 into the intervals of length d .

173 We choose the correlation time d to be equal to 1/2 of the mean duration of a
174 descending/ascending branch¹ of the secondary mutual event, i.e., the mean time
175 between the first and the second or between the third and the fourth contact. For
176 the observed events in Didymos, it is $d = 0.14$ h. (We also tested d to be twice as
177 long, i.e., equal to the full mean duration of the secondary event branch, but we
178 found it to be inadequate as the longer correlation time resulted in a substantial
179 loss of information by deweighting the datapoints too much.)

180 We note that the mutual orbit model fit is sensitive only to data points covering mu-
181 tual events and their closest neighborhood. Therefore we limited the above analysis
182 only to such data points; points further outside the events were not used, because
183 they do not effectively contribute to the determination of the mutual orbit.

184 Upon stepping a given parameter on a suitable interval (while the other parameters
185 fitted) and computing the normalized χ^2 for each step, we determined 3- σ uncer-
186 tainty of the given parameter as an interval in which χ^2 is below the p-value of the
187 χ^2 test, corresponding to the probability that the χ^2 exceeds a particular value only
188 by chance equal to 0.27%.

189 Plot of the normalized χ^2 vs ΔM_d is shown in Fig. 3. In order to save computing
190 time, the plots were constructed using spherical shapes for both components. How-
191 ever, a neighborhood of the best solution was then revisited using ellipsoidal shapes
192 in order to check the sensitivity of the solution to the shapes of the components. No
193 significant change of the solution was found for the polar flattening of the primary
194 up to 1.4 and the equatorial elongation of the secondary up to 1.5. We took these
195 values as the upper limits from Naidu et al., 2020 (the 3σ upper limit for the flat-
196 tening of the primary) and Pravec et al. 2016 (the upper limit for the elongation of
197 the secondary based on statistics of other small binary asteroids), respectively.

198 The long-period (orbital) lightcurve component data together with the synthetic
199 lightcurve of the best-fit solution are presented in Figs. 4 to 7. A close examination
200 of the figures reveals that while most of the observed events are fitted well, there are
201 some small or moderate discrepancies between the best-fit model and the data in
202 several mutual events. Those include (a) imprecisely modeled shapes of some primary
203 minima, (b) time offsets of some descending or ascending branches of the events or
204 (c) incorrect depths/lengths of some partial events. We ascribe these discrepancies
205 to the model simplifications, namely to the spherical or ellipsoidal approximation
206 of the shape of the primary. Local topography features on the disc (for the case a)
207 or on the limb (for the cases b and c) of the primary are suspected to be causes of
208 the respective effects.

209 The uncertainty area of the orbital pole is shown in Fig. 8. Figure 9 shows the

¹ We define a *branch* as a part of the mutual event in the lightcurve, where the brightness of the system is rapidly decreasing or increasing, i.e., the time period during which the eclipsed/occulted body is immersing into or emerging from the shadow of, or is disappearing behind or reappearing from behind the other body.

210 quadratic drift in the mean anomaly, ΔM , which was computed as follows. We
 211 generated a synthetic lightcurve using the model with parameters from the best-
 212 fit solution except ΔM_d , which was fixed at zero. Then, for each lightcurve event
 213 separately, we fitted the mean anomaly of the model in order to obtain the best
 214 match between its synthetic lightcurve and the observed data. ΔM is a difference
 215 between the mean anomaly of the original model and the fitted one. For each event,
 216 we computed also a standard deviation of ΔM using the procedure described above,
 217 but with χ^2 computed only from the data points in the vicinity of the mutual event
 218 in question.

219 3 Parameters of Didymos system

220 In this section, we summarize the best-fit model parameters of the Didymos binary
 221 system that we obtained or took from previous publications. The parameters are
 222 listed in Table 2.

223 In the first part of the table, we present data derived from optical and spectroscopic
 224 observations of the system. H_V and G are the mean absolute magnitude and the
 225 phase parameter of the H - G phase relation (Bowell et al., 1989). p_V is the visual
 226 geometric albedo derived by Naidu et al. (2020) using H_V and the effective diameter
 227 of the whole system from the 3D radar model.

228 Didymos is classified as an S-type asteroid (Cheng et al., 2018) based on vis-IR
 229 spectra obtained by de León et al. (2010).

230 In the next two parts of Table 2, we give parameters for the components of the
 231 binary. The indices 1 and 2 refer to the primary and the secondary, respectively.

232 **$D_{1,C}$ and $D_{2,C}$ are the mean (rotationally averaged) cross-section equiva-**
 233 **lent diameters (i.e., the diameter of a sphere with the same cross-section)**
 234 **of the primary and secondary, respectively, at the mean aspect of ob-**
 235 **served total secondary events (see below).**

236 To quantify the mean aspect we used an astero-centric latitude of the Phase Angle
 237 Bisector (PAB), which is the mean direction between the heliocentric and geocentric
 238 directions to the asteroid. As discussed in Harris et al. (1984), this is an approxi-
 239 mation for the effective viewing direction of an asteroid observed at the non-zero
 240 solar phase. **The average absolute value of the astero-centric latitude of the**
 241 **PAB for the observed total events was 9.7° . (We computed the latitude**
 242 **of the PAB using the nominal pole of the mutual orbit and assuming**
 243 **that the spin poles of both components are the same as the orbit pole.)**

244 $D_{1,V}$ and $D_{2,V}$ are the volume equivalent diameters (i.e., the diameter of a
 245 sphere with the same volume) of the primary and secondary, respectively.
 246 $D_{2,C}/D_{1,C}$ is the ratio between the mean cross-section equivalent diameters of the
 247 components. P_1 is the rotational period of the primary.

Table 2
Parameters of Didymos system

Parameter		Value	Unc.	Reference
Whole system:				
Absolute magnitude	H_V	18.16 ± 0.04	1σ	P12
Phase parameter	G	0.20 ± 0.02	1σ	K04
Visual geom. albedo	p_V	0.15 ± 0.04	1σ	N20
Taxon. class		S		C18
Primary:				
Volume equiv. diameter	$D_{1,V}$ (km)	0.780 ± 0.03	1σ	N20
Cross-section equiv. diameter	$D_{1,C}$ (km)	0.786 ± 0.05	1σ	This work/N20 ^a
Rotational period	P_1 (h)	2.2600 ± 0.0001	1σ	N20
Oblateness	$(A_1B_1)^{1/2}/C_1$	$1.04^{+0.12}_{-0.04}$	1σ	N20 ^b
Equatorial elongation	A_1/B_1	$1.02^{+0.09}_{-0.02}$	1σ	N20 ^b
Bulk density	ρ_1 (g cm ⁻³)	2.17 ± 0.35 / 2.44 ± 0.30	1σ	N20/ This work
Secondary:				
Cross-section equiv. diam. ratio	$D_{2,C}/D_{1,C}$	0.217 ± 0.004^c	1σ	This work
Cross-section equiv. diameter	$D_{2,C}$ (km)	0.171 ± 0.011	1σ	This work
Volume equiv. diameter	$D_{2,V}$ (km)	$\geq 0.171 \pm 0.011$	see text	This work
Mutual orbit:				
Sem. axis / primary diam.	$a/(A_1B_1)^{1/2}$	$1.59 \pm 0.20/1.51 \pm 0.22$	3σ	This work/N20 ^d
Semimajor axis	a (km)	1.19 ± 0.03	1σ	N20
Ecl. longitude of orbital pole	L_P (°)	320.6 ± 13.7^e	3σ	This work
Ecl. latitude of orbital pole	B_P (°)	-78.6 ± 1.8	3σ	This work
Drift in mean anomaly	ΔM_d (deg/yr ²)	0.15 ± 0.14	3σ	This work
Mean motion rate	\dot{n} (rad/s ²)	$5.26 \pm 4.91 \times 10^{-18}$	3σ	This work
Orbital period at t_0	P_{orb} (h)	11.921624 ± 0.000018	3σ	This work
Orbital period at t_{imp}	$\mathbf{P}_{\text{orb}}^{\text{imp}}$ (h)	11.921473 ± 0.000138	3σ	This work
Mean anomaly at t_0	M_0 (°)	89.1^f		This work
Eccentricity	e	≤ 0.03	3σ	SP09
Ecl. coordinates of the secondary wrt the primary at t_0				
	λ_0 (°)	320.7 ± 9.8^g	3σ	This work
	β_0 (°)	11.5 ± 1.9	3σ	This work
Epoch	t_0	JD 2455873.0 (asterocentric UTC)		
Ecl. coordinates of the secondary wrt the primary at t_{imp}				
	λ_{imp} (°)	222.8 ± 7.0^g	3σ	This work
	β_{imp} (°)	-1.6 ± 4.2	3σ	This work
Epoch of impact	t_{imp}	JD 2459849.46875 (geocentric UTC)		

References: C18: Cheng et al. 2018; K04: Kitazato et al. 2004; N20: Naidu et al. 2020; P12: Pravec et al. 2012; SP09: Scheirich and Pravec 2009.

^a Derived using shape model from N20, see text for details. ^b Derived using DEEVE from N20, see text for details. ^c This is a ratio of the cross-section equivalent diameters for the average observed aspect of 9.7°. See text for details. ^d Derived using DEEVE from N20, see text for details. ^e For the actual shape of the uncertainty area, see Fig. 8. Semiaxes of the area are $1.8 \times 3.0^\circ$. ^f We do not report the uncertainty of M_0 , since it is strongly correlated with L_P . Instead, we report uncertainties of λ_0 and β_0 . ^g For the actual shape of the uncertainty areas of λ_0 vs. β_0 and λ_{imp} vs. β_{imp} , see Fig. 10.

248 $(A_1 B_1)^{1/2}/C_1$ is a ratio between the mean equatorial and the polar axes of the
249 primary. A_1/B_1 is a ratio between the equatorial axes of the primary (equatorial
250 elongation). ρ_1 is the bulk density of the primary.

251 $D_{1,V}$ and the rotational period of the primary were taken from Naidu et al. (2020).
252 The cross-section equivalent diameter of the primary $D_{1,C}$ was computed from a
253 mean (rotationally averaged) cross-section of the radar shape model from Naidu et
254 al. (2020) at the mean aspect of the observed total events (asterocentric latitude
255 of the PAB being 9.7°). We adopted a 6% relative uncertainty for $D_{1,C}$. We note
256 that Naidu et al. (2020) give three uncertainties – 4% for the volume-equivalent
257 diameter of the primary, 6% for the extents along x and y principal axes of the
258 primary, and 10% for the extent along z-axis. The 6% uncertainty appears relevant
259 for our derivation of $D_{1,C}$.

260 We derived the secondary-to-primary mean cross-section equivalent diameter ratio
261 $D_{2,C}/D_{1,C}$ from the depths of the observed total secondary events. For that, we used
262 the high-quality data for the secondary events observed in November-December
263 2003, March 2019 and December 2020 (Pravec et al., 2022). The mean depth of
264 the total secondary events was measured to be 0.050 ± 0.002 mag, which gives
265 $D_{2,C}/D_{1,C} = 0.217 \pm 0.004$ (1- σ uncertainties).

266 From $D_{2,C}/D_{1,C}$ and $D_{1,C}$ we computed $D_{2,C}$. We note that Naidu et al. (2020)
267 reported visible extents of the secondary in the radar data of 150 ± 30 m, which is
268 consistent with our value.

269 To calculate the secondary volume equivalent diameter $D_{2,V}$ from the determined
270 secondary mean cross-section equivalent diameter $D_{2,C}$, we need to use a shape
271 model for the secondary. As Dimorphos' shape has not been determined yet, we
272 explore a range of possible ellipsoidal shapes for it. For a spherical secondary, we
273 have $D_{2,V} = D_{2,C}$. In a case the secondary is a prolate ellipsoid with $A_2/B_2 = 1.5$
274 and $B_2/C_2 = 1$ —we note that Pravec et al. (2016) found that the equatorial axis
275 ratios of NEA and small MBA binaries show an upper limit of A_2/B_2 about 1.5,
276 hence our choice of the extremally elongated ellipsoid here—, we obtain $D_{2,V} =$
277 0.173 ± 0.011 km. While we see here that the secondary volume equivalent diameter
278 is relatively insensitive to the equatorial axis ratio A_2/B_2 , it is more sensitive to
279 B_2/C_2 . Unfortunately there is no formal observational or theoretical constraint on
280 the B_2/C_2 for Dimorphos. To show the sensitivity of $D_{2,V}$ on the polar flattening
281 of the secondary, we calculate $D_{2,V}$ for an arbitrarily chosen value for B_2/C_2 of 1.5.
282 For a case of the oblate secondary with $A_2/B_2 = 1$ and $B_2/C_2 = 1.5$ we obtain
283 $D_{2,V} = 0.181 \pm 0.012$ km, while for a case of $A_2/B_2 = 1.5$ and $B_2/C_2 = 1.5$ we
284 obtain $D_{2,V} = 0.183 \pm 0.012$ km.

285 Other quantities reported above were taken or derived using data from other sources
286 as we describe in the following.

287 The mutual orbit and shapes of the Didymos components were modeled by Naidu
288 et al. (2020) from radar observations taken in 2003. They reported the size of the
289 primary to be close to a triaxial ellipsoid with axes $797 \times 783 \times 761$ m (1σ uncer-
290 tainties of $\pm 6\%$, 6% and 10% , respectively). The dimensions given are extents of

291 a dynamically equivalent equal-volume ellipsoid (DEEVE; a homogeneous ellipsoid
 292 having the same moments of inertia and volume as the shape model). We used these
 293 values to derive $(A_1 B_1)^{1/2}/C_1$ and A_1/B_1 .

294 The bulk density of the primary (which they assume is the same as the bulk density
 295 of the whole system) was taken from Naidu et al. (2020). For comparison, we derived
 296 the bulk density of the whole system from the mutual orbital elements obtained in
 297 our work, which leads to $2.44 \pm 0.30 \text{ g cm}^{-3}$ (1σ). **The derivation of the bulk**
 298 **density is as follows.**

299 **Assuming that both components have same bulk density, Kepler's third**
 300 **law can be written in the form (see Scheirich and Pravec, 2009)**

$$301 \quad \frac{4\pi^2}{GP_{\text{orb}}^2} \left[\frac{V_2}{V_1} + 1 \right]^{-1} \frac{a^3}{V_1} = \rho, \quad (3)$$

302 where ρ is the bulk density, G is the gravitational constant, V_2 and V_1
 303 are volumes of the secondary and the primary, respectively, a is the
 304 semimajor axis and P_{orb} is the orbital period. If the primary shape is
 305 assumed to be homogenous oblate ellipsoid and considering the effect of
 306 the oblateness up to the J_2 term (the first zonal harmonic coefficient in
 307 the gravitational potential expansion), the form can be modified to (see
 308 Rossi et al., 1999):

$$309 \quad \frac{4\pi^2 a^3}{GP_{\text{orb}}^{sid^2} (V_1 + V_2)} \epsilon = \rho, \quad (4)$$

310 where

$$311 \quad \epsilon = 1 - \frac{3}{10} \frac{A_1^2 - C_1^2}{a^2}, \quad (5)$$

312 where A_1 and C_1 are equatorial and polar axes of the primary, respec-
 313 tively.

314 The ellipsoidal approximation tends to overestimate the volume of the
 315 primary, and therefore our derived value of the bulk density should be
 316 considered rather as a lower limit. This compares to the estimates of the
 317 bulk densities of other S-type asteroids for which Scheeres et al. (2015)
 318 give an average value of $2.72 \pm 0.54 \text{ g cm}^{-3}$. Based on that, we suggest that
 319 the value of the bulk density of $2.17 \pm 0.35 \text{ g cm}^{-3}$, estimated by Naidu et
 320 al. (2020), may be underestimated.

321 In the last part of Table 2, we summarize the parameters of the mutual orbit of the
 322 binary components. a is the semimajor axis, L_P, B_P are the ecliptic coordinates of
 323 the orbital pole in the equinox J2000, and M_0 is the mean anomaly of the secondary,
 324 measured from the ascending node (as pericenter is not defined for circular orbit)
 325 for epoch $t_0 = 2455873.0$ (asterocentric UTC, i.e., light-time corrected). Since M_0

326 is strongly correlated with L_P , we report only its value for the nominal solution and
 327 do not report its uncertainty (which is on the same order as the uncertainty of L_P).
 328 Instead, to describe the uncertainty of the position of the secondary in its orbit as
 329 an independent parameter, we report its relative ecliptic coordinates with respect
 330 to the primary (see below).

331 e is the orbit eccentricity (only its upper limit is given, reported by Scheirich and
 332 Pravec 2009), and ΔM_d is the quadratic drift in the mean anomaly. Since the orbital
 333 period P_{orb} changes with time, the value presented in Table 2 is for the epoch t_0 .
 334 For this epoch, which is approximately the mean time of all observed events, a
 335 correlation between P_{orb} and ΔM_d is zero. We also give the time derivative of the
 336 mean motion \dot{n} , derived from ΔM_d , **and the value of the orbital period at the**
 337 **nominal time of the DART impact $P_{\text{orb}}^{\text{imp}}$.**

338 The uncertainty area of the orbit pole is shown in Fig. 8.

339 The relative semimajor axis given in Table 2 was derived using the assumption of
 340 spherical primary. To test the effect of flattening of the primary on a , we also fitted
 341 the data with $(A_1 B_1)^{1/2}/C_1$ fixed on three other values: 1.04, 1.16 and 1.40 (these
 342 were the nominal value, its 1σ upper limit and 3σ upper limit, respectively, taken
 343 from Naidu et al., 2020.). For these three values, we obtained following results for
 344 $a/(A_1 B_1)^{1/2}$: 1.60 ± 0.20 , 1.61 ± 0.20 and 1.63 ± 0.15 , respectively.

345 Naidu et al. (2020) give the value of the mutual semimajor axis to be 1.19 ± 0.03
 346 km (1σ). To compare their result with our value, we computed $a/(A_1 B_1)^{1/2}$ using
 347 their DEEVE for the primary and their semimajor axis of the mutual orbit. The
 348 result is given in Table 2.

349 λ_0 and β_0 are relative ecliptic coordinates of the secondary with respect to the
 350 primary at the epoch t_0 . For the nominal time of the DART impact ($t_{\text{imp}} = 2022$ -
 351 09-26.96875 geocentric UTC), these coordinates are given by λ_{imp} and β_{imp} .

352 Note that the uncertainty of λ_{imp} is smaller than the uncertainty of λ_0 . This is
 353 because of the following: The time evolution of the uncertainty of λ is governed
 354 primarily by two factors: a) at the epochs covered with the data, it is restricted by
 355 their amount and quality; b) it grows quadratically into the future from the last
 356 observed apparition. Therefore, the uncertainty is small at the first and the last
 357 apparition (panels **a** and **c** on Fig. 10), while at t_0 , which is not covered by the
 358 data, the uncertainty is larger (panel **b** on Fig. 10). The last panel (**d**) of Fig. 10
 359 shows the uncertainty at the nominal time of the DART impact. To demonstrate
 360 the change of the uncertainty more illustratively, we constructed Fig. 11 showing
 361 an evolution of the $3\text{-}\sigma$ uncertainty of λ in time.

362 **Although assuming that the Dimorphos orbit is coplanar with the pri-**
 363 **mary's equator throughout the modeling presented above, we also exam-**
 364 **ined the possibility that this assumption is not held. We obtained that**
 365 **the inclination of the Dimorphos orbit to the primary's equator is $\lesssim 3^\circ$**
 366 **(see Appendix A).**

367 *3.1 The inward drift of the mutual orbit*

368 The mean anomaly of a changing orbit expanded to the second degree in
 369 time is expressed by Equations (1) and (2). ΔM_d can be expressed using
 370 a semimajor axis of the mutual orbit a and its time derivative as

$$371 \quad \Delta M_d = \frac{1}{2} \dot{n} = -\frac{3n\dot{a}}{4a}. \quad (6)$$

372 The observed value of $\Delta M_d = 0.15 \pm 0.14$ deg/yr² therefore imply an inward
 373 semimajor axis drift at the rate of $\dot{a} = -0.09 \pm 0.08$ cm/yr (3σ uncertainty).

374 Didymos system is the fourth binary for which we now have a long-
 375 term dynamical evolution inferred. The other three are (175706) 1996
 376 FG3 that has a mean anomaly drift consistent with zero ($\Delta M_d = 0.04 \pm$
 377 0.20 deg/yr², Scheirich et al., 2015), (66391) Moshup that shows an out-
 378 ward drift of the mutual orbit ($\Delta M_d = -0.65 \pm 0.16$ deg/yr², Scheirich et
 379 al., 2021), and (88710) 2001 SL9 that shows an inward drift of the mutual
 380 orbit (two solutions for ΔM_d : 2.8 ± 0.2 or 5.2 ± 0.2 deg/yr², Scheirich et al.,
 381 2021).

382 In the following, we discuss two possible mechanisms that can explain
 383 the slow inward drift of the Didymos system.

384 *a) BYORP and tides*

385 The binary YORP (BYORP) effect is a secular change of the mutual
 386 orbit of a binary asteroid system with a synchronous satellite due to
 387 the emission of thermal radiation from the asymmetric shape of that
 388 satellite. It was first hypothesized by Čuk and Burns (2005). McMahon
 389 and Scheeres (2010a,b) built a detailed theory of the secular evolution of
 390 the mutual orbit due to the BYORP effect, which predicts that it causes
 391 the orbit to expand or contract on a timescale of thousands of years, as
 392 long as the satellite remains synchronous.

393 Adapting the method derived by McMahon and Scheeres (2010b), Pravec
 394 and Scheirich (2010) predicted² the quadratic drift of (65803) Didy-
 395 mos caused by BYORP to be 2.51 deg/yr². Our detected value, $0.15 \pm$
 396 0.14 deg/yr² is much lower than this estimate. More recently, Jacob-
 397 son and Scheeres (2011) presented an improved theory that incorporates
 398 both the BYORP effect and mutual tides between the two components.
 399 They showed that a stable long-term equilibrium may exist between these
 400 two torques if the BYORP effect is removing angular momentum from
 401 the orbit. Since the rotation period of Didymos is shorter than the or-
 402 bital period of Dimorphos, the satellite raises a tidal bulge on the primary

² This value of ΔM_d is based on a shape model of a secondary of another NEA binary – (66391) Moshup – and it is only a magnitude, not directional estimate.

403 that removes energy from the rotation of the primary and transfers an-
404 gular momentum to the mutual orbit. These two torques are opposite
405 in sign and can balance one another because they depend differently on
406 the mutual orbit semi-major axis. They evolve the mutual orbit to an
407 equilibrium semi-major axis, where the mutual orbit no longer evolves
408 (Scheirich et al., 2015, reported the first binary system observed to be
409 in or very close to this equilibrium state).

410 The observed low positive value of the mean anomaly drift of Didymos
411 may indicate that the system is evolving into and it is very close to,
412 however not yet exactly at, such equilibrium.

413 *b) Differential Yarkovsky force in binary asteroid system*

414 Another effect causing a drift of the mutual semimajor axis is the Yarkovsky
415 force, which affects not only the motion of the center of mass of the whole
416 binary system but also the relative motion of components (Vokrouhlický
417 et al., 2005). For NEA binaries, the semimajor axis drift is on the order
418 from ~ 0.1 mm/yr to several mm/yr (Scheirich et al., 2021), i.e., on the
419 same order as the drift observed in the Didymos system. Besides the
420 BYORP, the differential Yarkovsky force is therefore another possible
421 mechanism explaining the drift.

422 4 Mutual events prediction for the 2022–2023 apparition

423 In order to facilitate planning ground-based observations before and after the DART
424 impact, we computed times of mutual events that will occur in the 2022–2023 ap-
425 parition using the nominal solution presented in Section 3. It is available at
426 https://asu.cas.cz/~asteroid/Didymos_2022-2023_events.htm.

427 The **list also includes** the events for a period after the DART impact. Since the
428 prediction in this period is made using the assumption that none of the orbital
429 parameters will change, it has an informative character only.

430 5 Conclusions

431 The near-Earth asteroid (65803) Didymos is among the best characterized small
432 asteroid binary systems. It is a typical member of the population of near-Earth
433 asteroid binaries for most of its parameters. With the photometric data taken during
434 five apparitions over the time interval of 17 years, we constrained its binary orbit
435 and determined the **relative** position of its secondary (Dimorphos) at the time of
436 the DART impact to within $\pm 7.0^\circ$ (3σ uncertainty) **with respect to the primary**.

437 We found that the mean motion of Dimorphos is increasing with a rate of $\dot{n} =$
438 $5.26 \pm 4.91 \times 10^{-18}$ rad/s² (3σ uncertainty), implying that the mutual semimajor
439 axis is shrinking in time. After the near-Earth binary asteroid (88710) 2001 SL9
440 (Scheirich et al., 2021), this is the second case with this observed property. As the
441 inward drift of its orbit can not be explained by mutual tides for the system with
442 the rotation period of the primary shorter than the orbital period of the secondary
443 (assuming the same sense of primary rotation and the mutual orbital
444 motion), it suggests that either an interplay between the binary YORP
445 (BYORP) effect and mutual tides, or the differential Yarkovsky force, or
446 a combination of these effects, acts in the Didymos system.

447 Appendix A. Assessment of the mutual orbit nodal precession

448 In Section 2.2, the spin axis of the primary was assumed to be normal to
449 the mutual orbital plane of the components. Here we examine if this as-
450 sumption is reasonable and how the primary spin axis orientation affects
451 the results.

452 In the case of spherical primary, the orientation of its spin axis has no
453 effect either on the model lightcurve nor the results. In the case of an
454 oblate primary, the main issue is that the orbital pole precedes around
455 the spin pole of the primary when the two poles are not same. The
456 nodal precession rate depends on the oblateness of the primary and other
457 system parameters (see, e.g., Rossi et al., 1999). We tested three values
458 of the primary oblateness: 1.04, 1.16 and 1.40 (i.e. the nominal value
459 from Naidu et al. 2020 and its 1σ and 3σ upper limits, respectively).
460 For these three values, the nodal precession rates are -1.61 , -5.50 and
461 $-10.57^\circ/\text{day}$, respectively (we neglect the dependence of the nodal rate
462 on the inclination of the satellite's orbit to the primary's equator because
463 it is negligible for small angles).

464 We tested twelve orientations of the spin axis with respect to the orbital
465 axis: four different orientations with an inclination between the axes of 1° ,
466 four with the inclination of 2° , and four with 4° . (The four orientations of
467 the spin axis correspond to four different values of the length of ascending
468 node of the satellite's orbit with respect to the primary's equator at the
469 reference epoch.) For each combination of the orientation of the spin
470 axis and the oblateness of the primary (the corresponding nodal rate

471 was used for each oblateness), we then re-run the analysis.

472 From the best-fit solutions with inclinations of 1° , the largest absolute
473 differences in parameters with respect to the nominal solution were: the
474 difference in the mutual semimajor axis $\delta a/(A_1 B_1)^{1/2} = 0.07$, the difference
475 in the orbital period $\delta P_{\text{orb}} = 0.00000072$ h, the difference in the mean
476 anomaly drift rate $\delta \Delta M_d = 0.016$ deg/yr², the differences in the relative
477 ecliptic coordinates of the secondary with respect to the primary at the
478 nominal time of the DART impact $\delta \lambda_{\text{imp}} = 1.2^\circ$, $\delta \beta_{\text{imp}} = 0.7^\circ$.

479 From the best-fit solutions with inclinations of 2° , the largest absolute
480 differences in parameters with respect to the nominal solution were:
481 $\delta a/(A_1 B_1)^{1/2} = 0.11$, $\delta P_{\text{orb}} = 0.00000096$ h, $\delta \Delta M_d = 0.016$ deg/yr², $\delta \lambda_{\text{imp}} = 1.0^\circ$,
482 $\delta \beta_{\text{imp}} = 1.5^\circ$.

483 The best-fit solutions with inclinations of 4° are all inconsistent with the
484 observed data. We obtain that the inclination of the Dimorphos orbit to
485 the primary's equator is $\lesssim 3^\circ$.

486 References

487 Bowell, E., Hapke, B., Domingue, D., Lumme, K., Peltoniemi, J., Harris, A.W.,
488 1989. Application of photometric models to asteroids. In: Asteroids II. Univ. Arizona
489 Press, pp. 524-556.

490 Cheng, A.F., et al., 2015. Asteroid impact and deflection assessment
491 mission. *Acta Astronaut.* **115**, 262–269.

492 Cheng, A.F., Rivkin, A.S., Michel, P., Atchison, J., Barnouin, O., Benner, L.,
493 Chabot, N.L., Ernst, C., Fahnestock, E.G., Kueppers, M., Pravec, P., Rainey, E.,
494 Richardson, D.C., Stickle, A.M., Thomas, C., 2018. AIDA DART asteroid deflection
495 test: planetary defense and science objectives. *Planet. Space Sci.* **157**, 104115.

496 de León, J., Licandro, J., Serra-Ricart, M., Pinilla-Alonso, N., Campins, H., 2010.
497 Observations compositional, and physical characterization of near-Earth and Marscrosser
498 asteroids from a spectroscopic survey. *A&A* **517**, A23. <https://doi.org/10.1051/0004-6361/200913852>.

500 Dunn, T.L., Burbine, T.H., Bottke, W.F., Jr, Clark, J.P. 2013. Mineralogies and
501 source regions of near-Earth asteroids. *Icarus*, **222**, 273–282.

502 Harris, A.W., Young, J.W., Scaltriti, F., Zappalà, V., 1984. Lightcurves and phase
503 relations of the Asteroids 82 Alkmene and 444 Gyptis. *Icarus* **57**, 251258.

504 Jacobson, S.A., Scheeres, D.J., 2011. Long-term Stable Equilibria for
505 Synchronous Binary Asteroids. *ApJ Letters*, **736**, L19.

506 Kaasalainen, M., Torppa, J., 2001. Optimization Methods for Asteroid
507 Lightcurve Inversion. I. Shape Determination. *Icarus*, **153**, 24

- 508 Kitazato, K., Abe, M., Mito, H., Tarusawa, K., Soyano, T., Nishihara, S., Sarugaku,
509 Y., 2004. Photometric behaviour dependent on solar phase angle and physical char-
510 aracteristics of binary near-Earth Asteroid (65803) 1996 GT. *Lunar Planet. Sci.* 35.
511 Abstract 1623
- 512 McMahon, J., Scheeres, D., 2010a. Secular orbit variation due to solar radiation
513 effects: a detailed model for BYORP. *Celest. Mech. Dyn. Astron.* 106, 261300.
- 514 McMahon, J., Scheeres, D., 2010b. Detailed prediction for the BYORP effect on
515 binary near-Earth Asteroid (66391) 1999 KW4 and implications for the binary pop-
516 ulation. *Icarus*, 209, 494–509.
- 517 Michel, P., Kueppers, M., Campo Bagatin, A., et al. 2022. PSJ, submitted.
- 518 Naidu, S. P. et al. 2020. Radar observations and a physical model of binary near-
519 earth asteroid 65803 Didymos, target of the DART mission, *Icarus* 348, 113777
- 520 **Naidu, S. P. et al. 2022. Anticipating the DART impact: Orbit estimation**
521 **of Dimorphos using a simplified model. Submitted to Planetary Science**
522 **Journal.**
- 523 Pravec, P., Benner, L. A. M., Nolan, M. C., et al. 2003, IAUC, 8244.
- 524 Pravec, P., et al., 2006, Photometric survey of binary near-Earth asteroids, *Icarus*,
525 181:6393.
- 526 Pravec, P., Harris, A.W., 2007. Binary asteroid population. 1: Angular momentum
527 content. *Icarus* 190, 250-259.
- 528 **Pravec, P., Scheirich, P., 2010. Binary System Candidates for Detection**
529 **of BYORP. 42nd annual meeting of the Division for Planetary Sciences**
530 **of the American Astronomical Society, Oct. 3 - Oct. 8, 2010, Pasadena,**
531 **CA.**
- 532 Pravec, P., et al. 2012. Absolute magnitudes of asteroids and a revision of asteroid
533 albedo estimates from WISE thermal observations, *Icarus* 221, 365-387.
- 534 Pravec, P., et al. 2022. Photometric observations of the binary near-Earth asteroid
535 (65803) Didymos in 2015-2021 prior to DART impact. Submitted to Planetary
536 Science Journal.
- 537 Rivkin, A. S., Chabot, N. L., Stickle, A. M., et al. 2021, PSJ, 2, 173
- 538 **Rossi, A., Marzari, F., Farinella, P. 1999. Orbital evolution around irreg-**
539 **ular bodies. Earth, Planets and Space** 51, 1173-1180.
- 540 **Scheeres D. J., Britt D., Carry B., and Holsapple K. A. (2015) Asteroid**
541 **interiors and morphology. In Asteroids IV (P. Michel et al., eds.), pp.**
542 **745766. Univ. of Arizona, Tucson.**
- 543 Scheirich, P., and Pravec, P., 2009. Modeling of lightcurves of binary asteroids,

544 Icarus, 200:531547.

545 Scheirich, P., Pravec, P., Jacobson, S. A., Ďurech, J., Kušnirák, P.,
546 Hornoch, K., Mottola, S., Mommert, M., Hellmich, S., Pray, D., Pol-
547 ishock, D., Krugly, Y. N., Inasaridze, R. Y., Kvaratskhelia, O. I., Ay-
548 vazian, V., Slyusarev, I., Pittichová, J., Jehin, E., Manfroid, J., Gillon,
549 M., Galád, A., Pollock, J., Licandro, J., Alí-Lagoa, V., Brinsfield, J.,
550 Molotov, I. E., 2015. The binary near-Earth Asteroid (175706) 1996 FG₃
551 – An observational constraint on its orbital evolution. *Icarus*, 245, 56–63.

552 Scheirich, P. and 36 colleagues, 2021. A satellite orbit drift in binary near-Earth
553 asteroids (66391) 1999 KW4 and (88710) 2001 SL9 - Indication of the BYORP
554 effect, *Icarus* 360. doi:10.1016/j.icarus.2021.114321

555 Vokrouhlický, D., Čapek, D., Chesley, S. R., Ostro, S. J., 2005. Yarkovsky detection
556 opportunities. II. Binary systems. *Icarus*, 179, 128–138

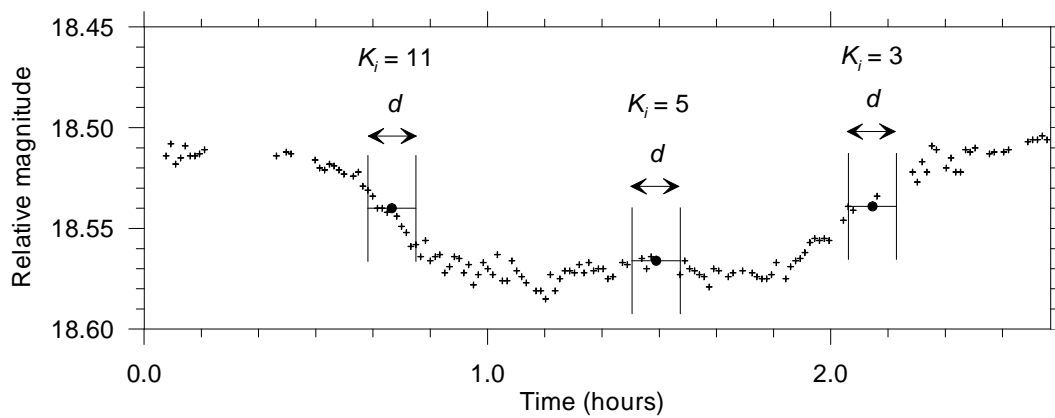


Fig. 1. An example of the determination of the weights applied to individual data points, as described in Section 2.2. The observed data are marked as crosses. For each data point, the number K_i of all data points that are within $\pm d/2$ from the given point is calculated (for the three examples shown, $K_i = 11, 5$ and 3). d is the correlation time, which we set equal to 0.14 h. A contribution of each data point to the χ^2 sum is then weighted by $1/K_i$.

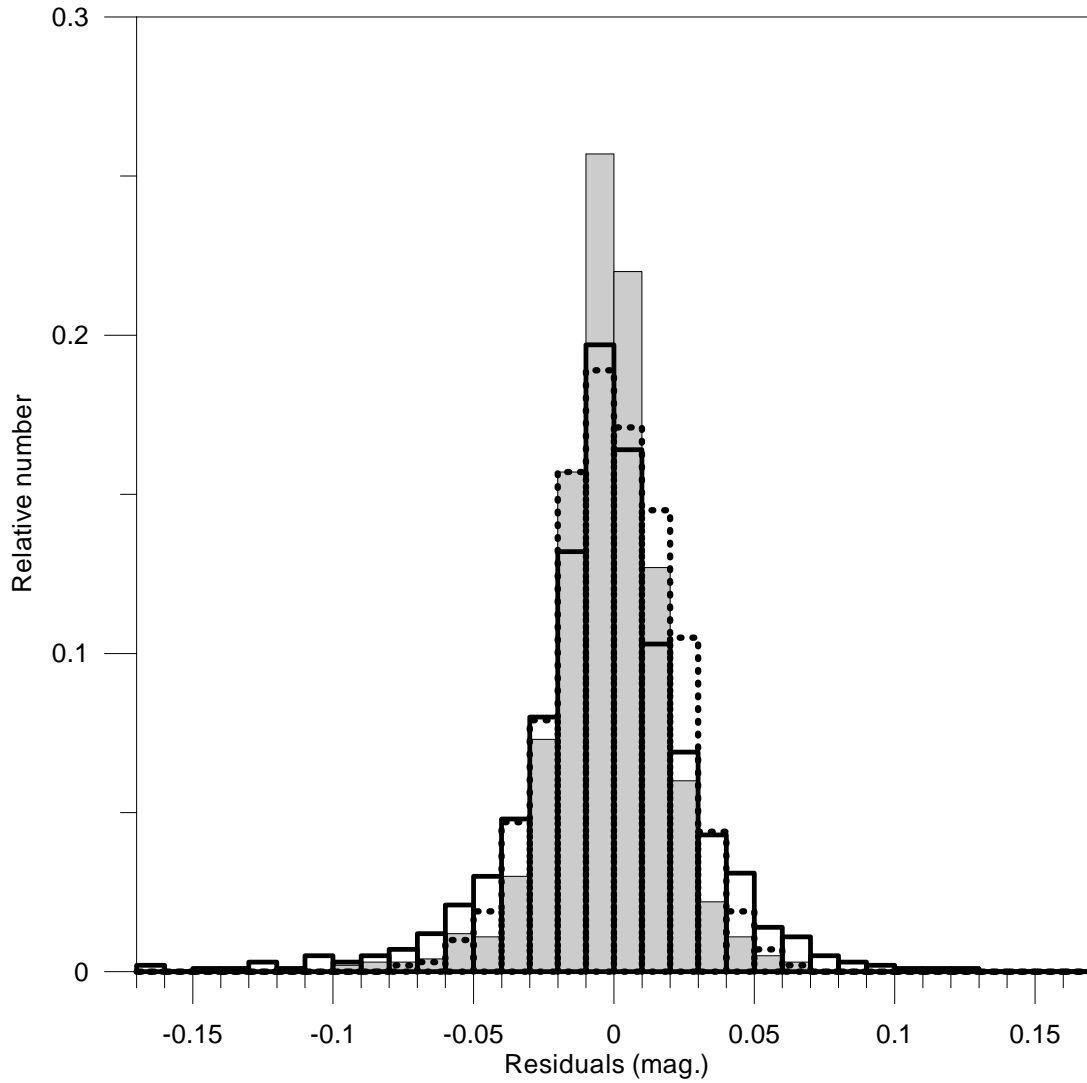


Fig. 2. Distribution of residuals of the model fitted to the observational data without the application of weights described in Section 2.2 (grey area) and with the weights applied (thick solid line). A histogram of a set of randomly generated values with normal distribution and standard deviation of 0.0216 mag. (thick dotted line) is shown for comparison.

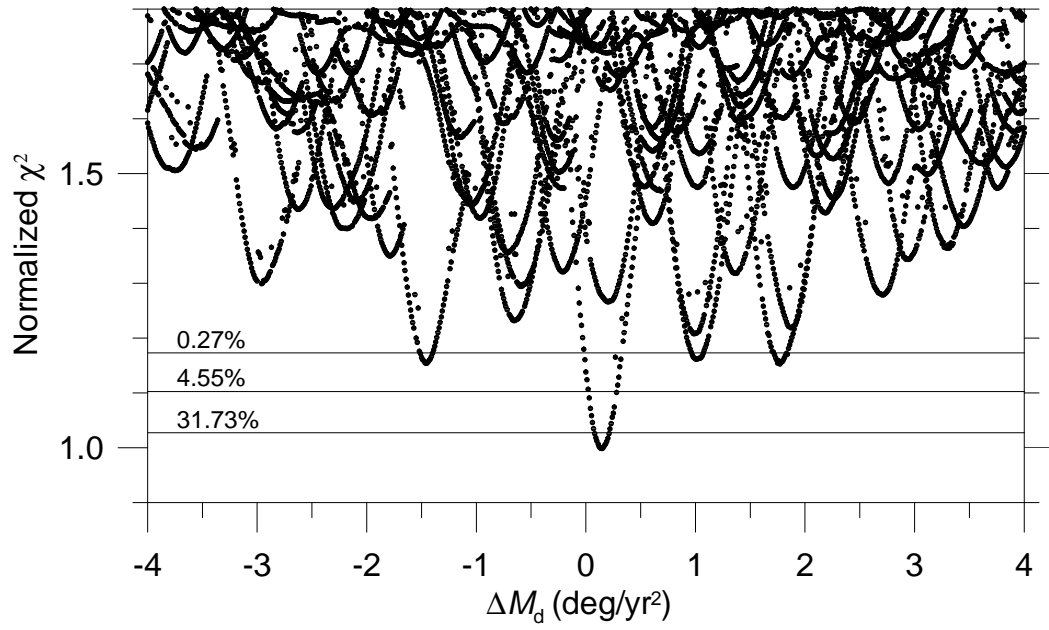


Fig. 3. The normalized χ^2 vs. ΔM_d for solutions of the model presented in Section 2.2. The three horizontal lines give the p-values – the probabilities that the χ^2 exceeds a particular value only by chance, corresponding to 1-, 2- and 3σ interval of the χ^2 distribution with 567 degrees of freedom. See text for details.

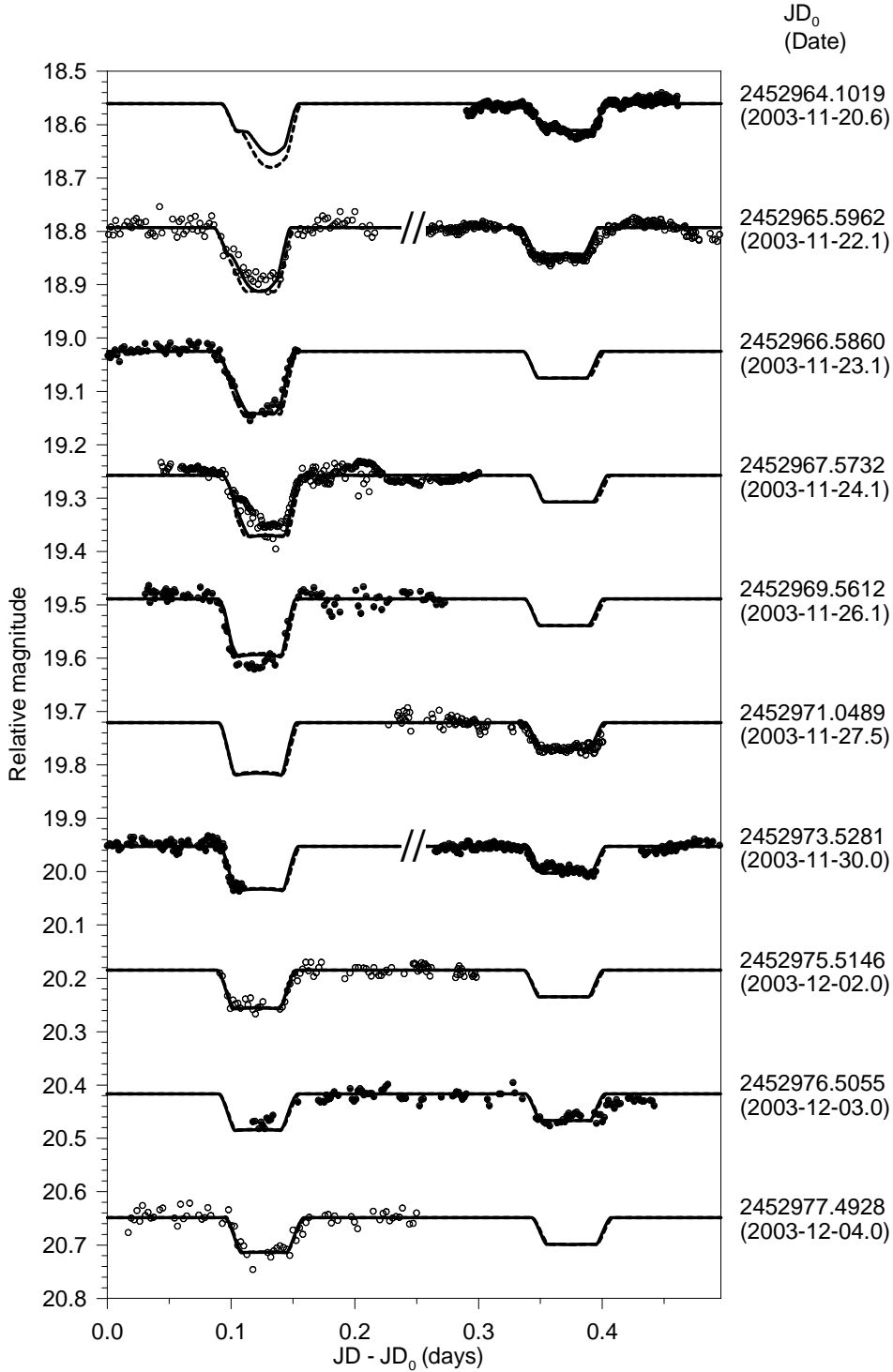


Fig. 4. The orbital lightcurve component of the Didymos system. The observed data are marked as points. (To avoid confusion between different data sets, solid and empty symbols are used alternating on each plot.) The solid curve represents the synthetic lightcurve for the best-fit solution. For comparison, the dashed curve is the model with ΔM_d fixed at 0.0 deg/yr² and all other parameters varied to obtain the best fit. The primary and secondary events (the terms refer to which of the two bodies is occulted or eclipsed) are always shown on the left and right side of the plots, respectively. In some cases, the observations of a secondary event precede that of a primary event (i.e., their order in the dataset is inverse of that shown on the plot). In order to save space in the plot, we present these events in reverse order to how they were observed. They are separated by “//” symbol in the plot and one orbital period (0.496 d) is to be subtracted from x coordinate of data points to the right from this separator.

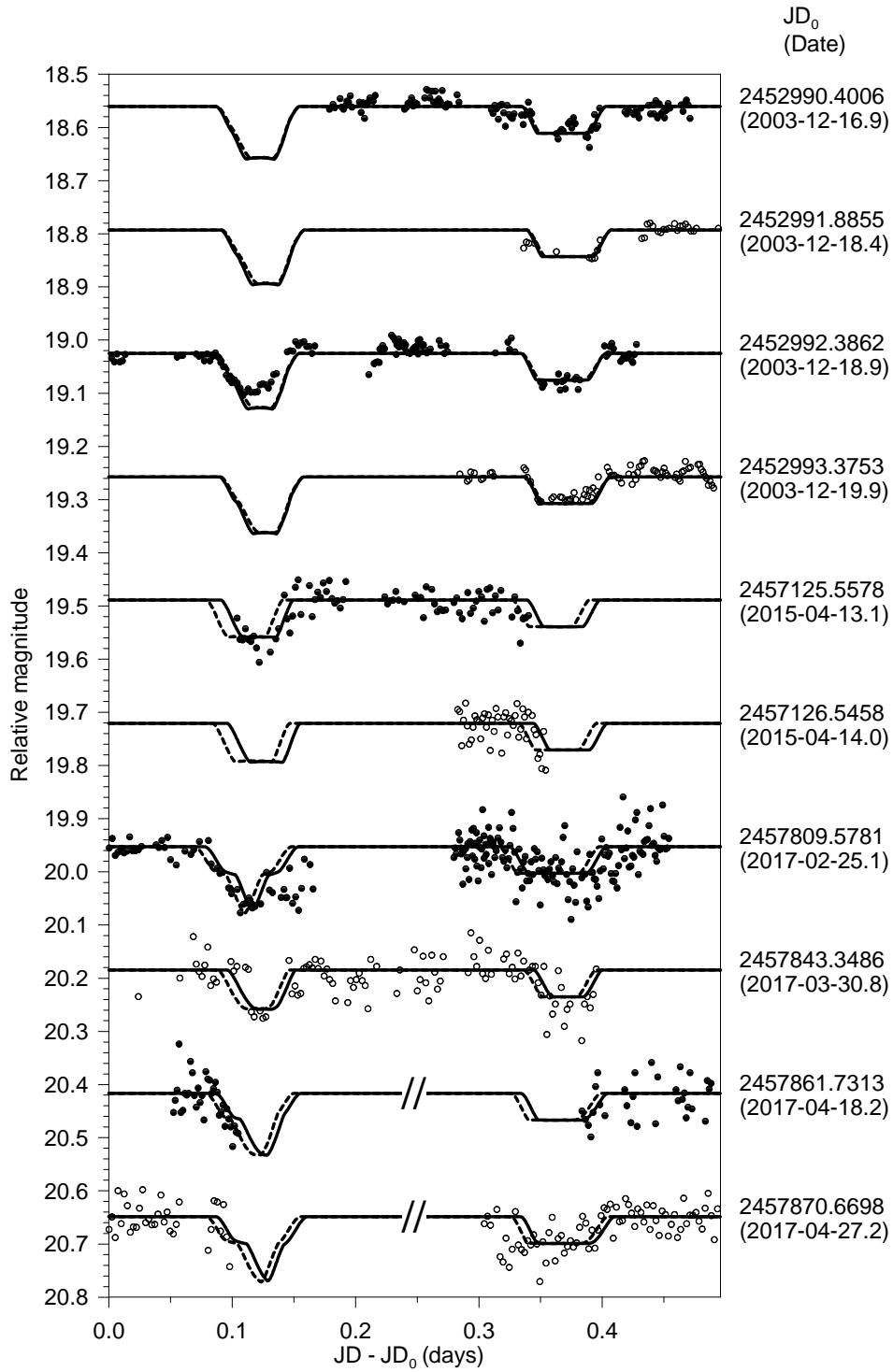


Fig. 5. Continuation of Fig. 4.

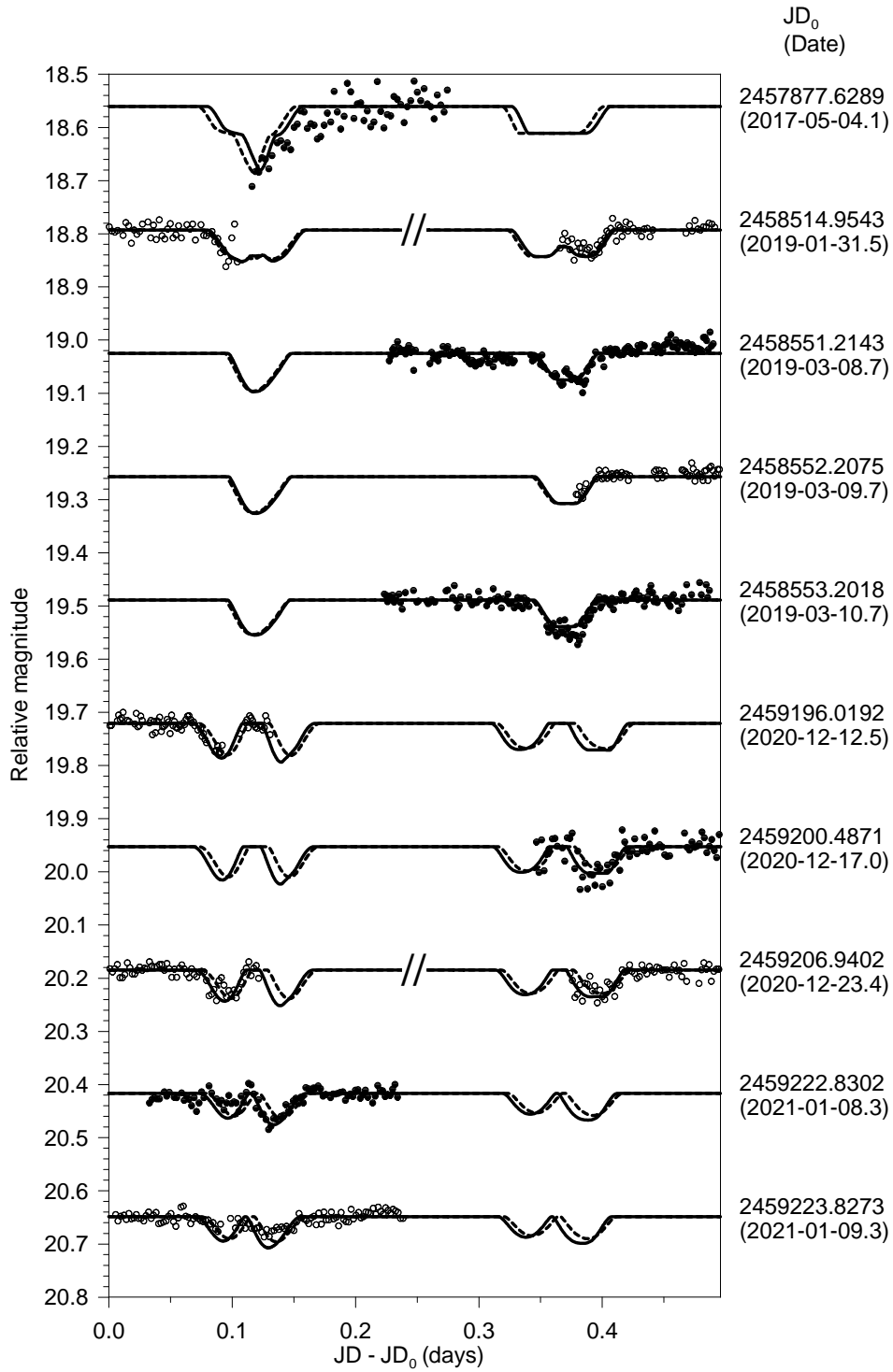


Fig. 6. Continuation of Fig. 4.

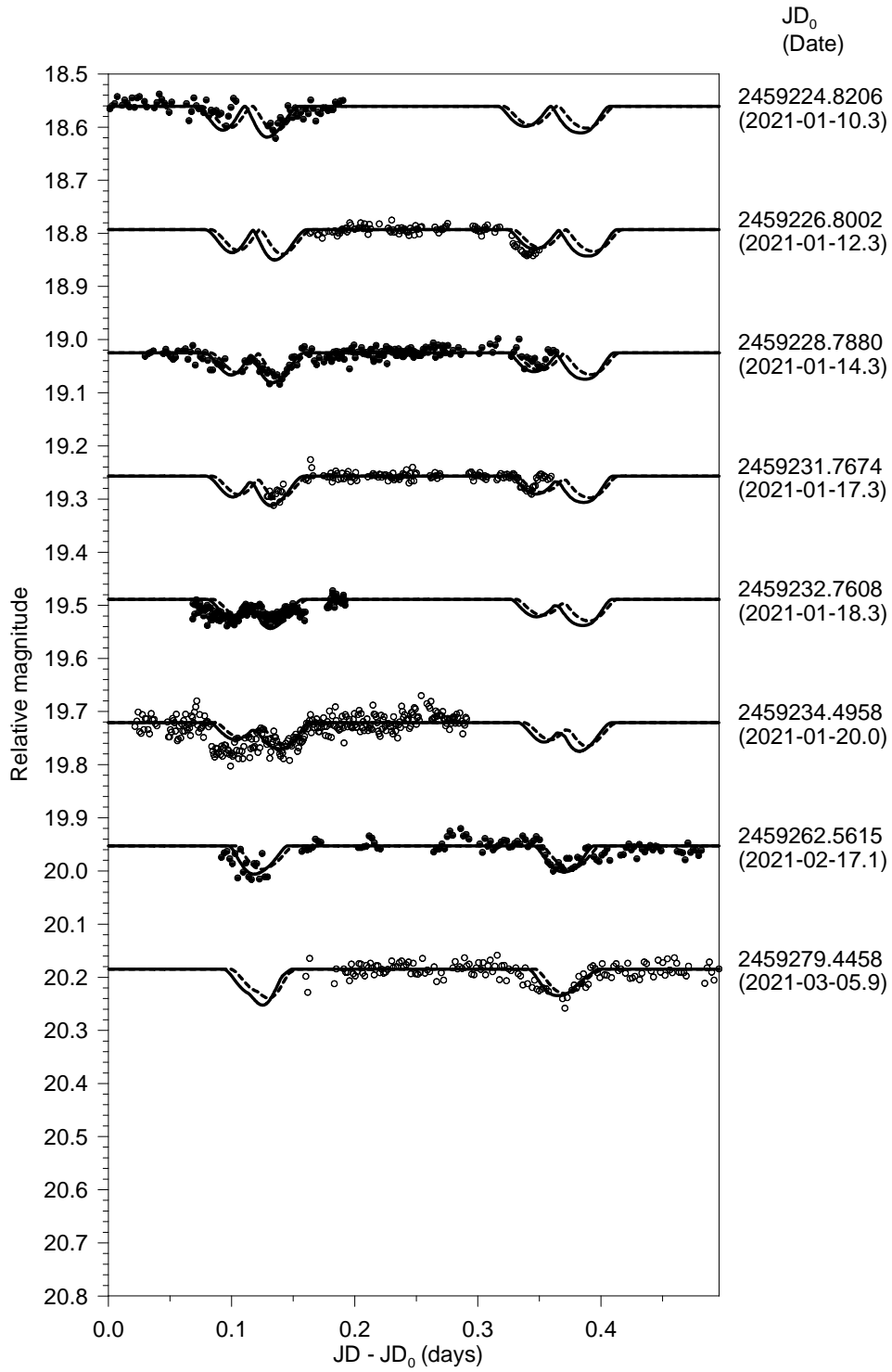


Fig. 7. Continuation of Fig. 4.

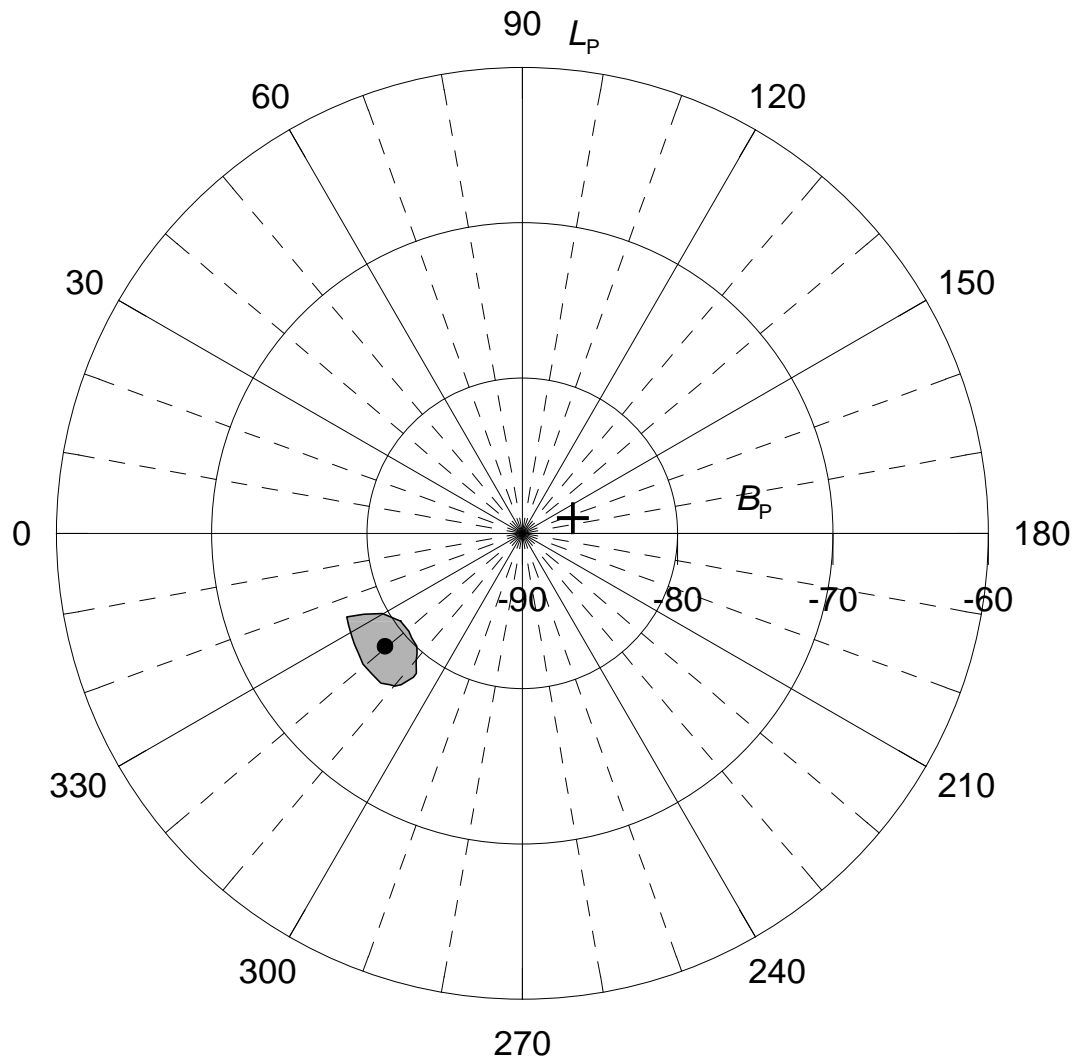


Fig. 8. Area of admissible poles for the mutual orbit of Didymos in ecliptic coordinates (grey area). The dot is the nominal solution given in Table 2. This area corresponds to 3σ confidence level. The south pole of the current asteroid's heliocentric orbit is marked with the cross.

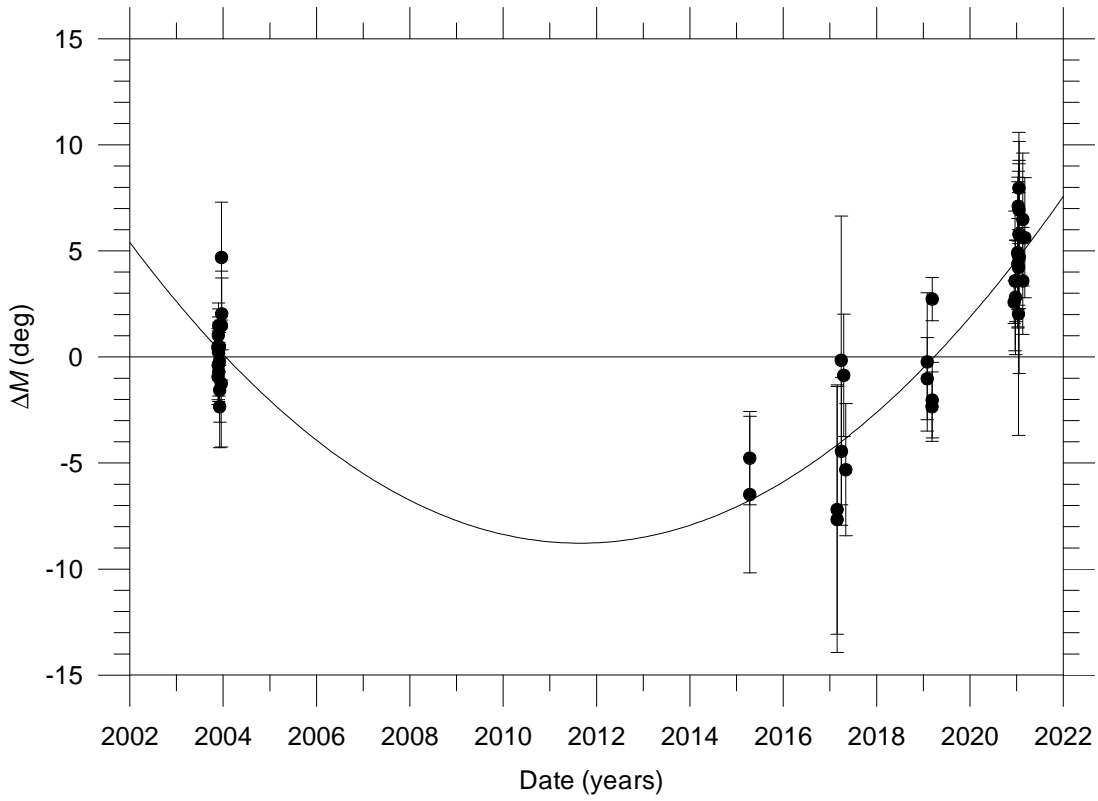


Fig. 9. Time evolution of the mean anomaly difference ΔM with respect to the solution with $\Delta M_d = 0$. See text for details. Each point corresponds to a mutual event covered by the observed data. Vertical error bars represent estimated 1σ uncertainties of the event times, expressed in the mean anomaly. A quadratic fit to the data points, represented by the solid curve, gives the quadratic term of 0.152 deg/yr^2 .

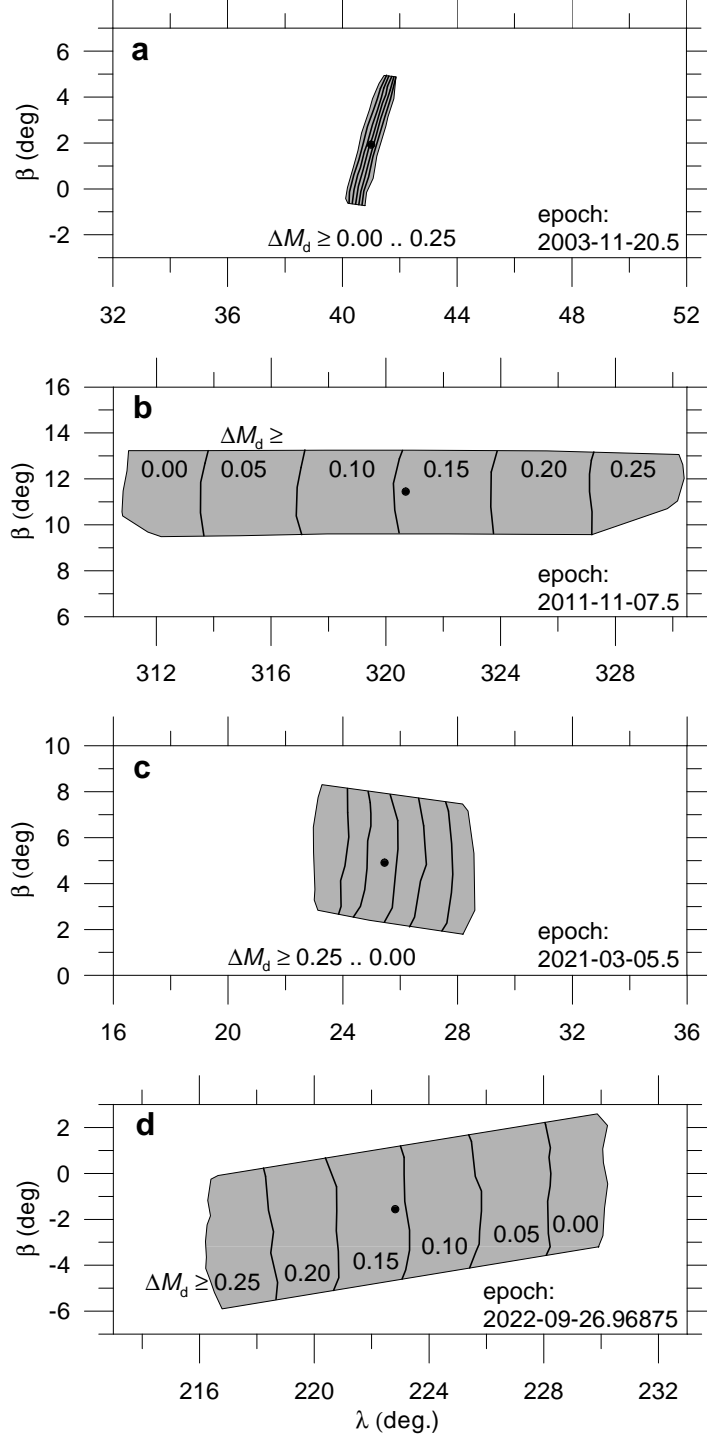


Fig. 10. $3\text{-}\sigma$ uncertainty area of Dimorphos relative position with respect to Didymos expressed in ecliptical coordinates λ , β (grey areas). To demonstrate the change in size of the uncertainty area with time, we plotted the area for four epochs (2003-11-20.5 – the beginning of the first apparition in 2003; 2011-11-07.5 – epoch JD0; 2021-03-05.5 – the end of the last apparition in 2021; 2022-09-26.96875 – the nominal epoch of the DART impact; panels a, b, c, d, respectively) with the same scale of the axes on all four panels. To show a correlation between λ and ΔM_d , the approximately vertical lines divide areas with $\Delta M_d \geq 0.00; 0.05; 0.10; 0.15; 0.20; 0.25$ deg/yr², respectively (the inequality is used because ΔM_d is correlated with other parameters as well and therefore strict boundaries for its values cannot be given). The dots denote the nominal solution given in Table 2.

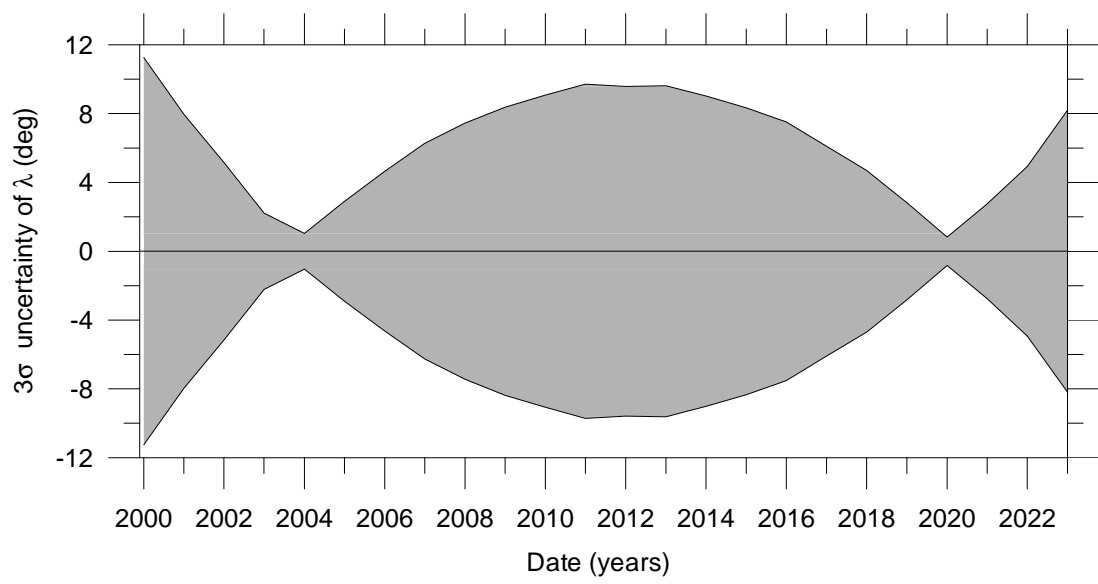


Fig. 11. Evolution of the 3- σ uncertainty of the ecliptic longitude (λ) of the radius vector of Dimorphos with respect to Didymos in time.